

Lab on a Chip

Accepted Manuscript

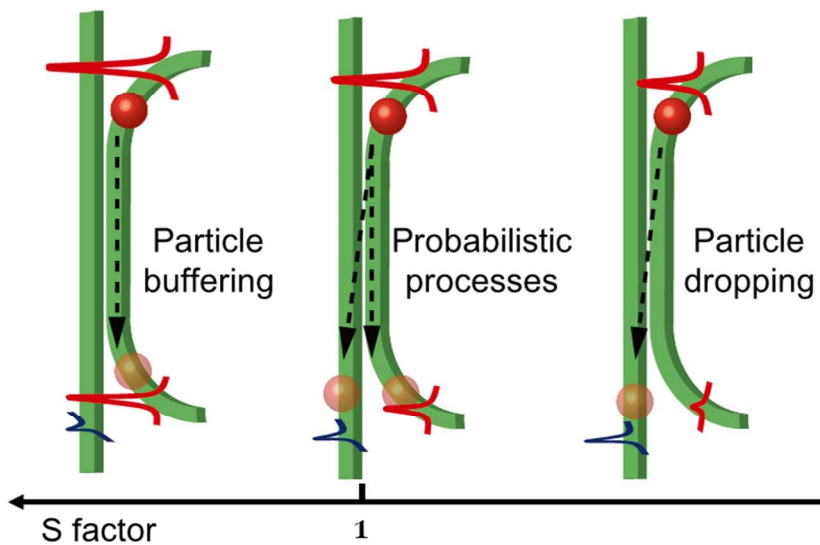


This is an *Accepted Manuscript*, which has been through the Royal Society of Chemistry peer review process and has been accepted for publication.

Accepted Manuscripts are published online shortly after acceptance, before technical editing, formatting and proof reading. Using this free service, authors can make their results available to the community, in citable form, before we publish the edited article. We will replace this *Accepted Manuscript* with the edited and formatted *Advance Article* as soon as it is available.

You can find more information about *Accepted Manuscripts* in the [Information for Authors](#).

Please note that technical editing may introduce minor changes to the text and/or graphics, which may alter content. The journal's standard [Terms & Conditions](#) and the [Ethical guidelines](#) still apply. In no event shall the Royal Society of Chemistry be held responsible for any errors or omissions in this *Accepted Manuscript* or any consequences arising from the use of any information it contains.



254x190mm (96 x 96 DPI)

We propose and demonstrate a design rule for determining microparticle buffering and dropping in microring-resonator-based add-drop devices at cavity resonances.

ARTICLE

Unfolding a design rule for microparticle buffering and dropping in microring-resonator-based add-drop devices

Cite this: DOI: 10.1039/x0xx00000x

Jiawei Wang and Andrew W. Poon

Received 00th January 2012,
Accepted 00th January 2012

DOI: 10.1039/x0xx00000x

www.rsc.org/

We propose an intuitive and quantitative design rule to determine the microparticle transport processes, including buffering and dropping, on microring-resonator-based add-drop devices at cavity resonances in an integrated optofluidic chip. The design rule uses the splitting ratio, S , of the optical-field intensity at the microring-feedback-arc just after the output-coupling region to that at the drop-waveguide as a figure-of-merit for particle transport to determine between particle buffering ($S > 1$) and dropping ($S < 1$). The particle transport, however, becomes probabilistic in the case that S is close to 1. The S factor thus provides a clearer physical criterion for determining the particle transport processes compared to the cavity quality (Q) factor. We experimentally investigate this design rule on four different devices with different design parameters on a silicon nitride-on-silica substrate, and show that the particle transport behaviours of 2.2 μm - and 0.8 μm -sized polystyrene particles are consistent with the S values extracted from the transmission spectra. Our numerical simulations of the four devices suggest that the S values extracted from the simulated transmission spectra are consistent with those extracted from the simulated mode-field intensity distributions. We calculate the optical field using Maxwell stress tensor and an effective microdisk model to relate the S values to the particle transport processes. We further experimentally demonstrate the viability of the design rule by switching between deterministic particle buffering and probabilistic particle transport processes by switching the polarization modes.

Introduction

Applying optical surface waves of on-chip integrated optical devices for micro/nano-sized particle and biological cell manipulation has been gaining increasing interests in the research field of optofluidics for lab-on-a-chip applications. In comparison with the conventional free-space optical tweezers¹⁻³, on-chip optical manipulation offers mass particle transport using relatively low optical power.⁴⁻⁶ Over the past few years, various research groups have studied on-chip optical manipulation of micro- and nano-sized particles using optical microresonators and nanoresonators, including travelling-wave microring⁷⁻¹⁰ and microdisk¹¹ resonators and standing-wave one-dimensional photonic crystal nanoresonators¹²⁻¹⁶ for their key merits of high resonant cavity-field enhancement and the possibility of wavelength-tunable particle manipulation near sharp resonances. Specifically, Yang, et al.,⁷ and Lin, et al.,⁸ demonstrated micron-sized polystyrene particle trapping and

transport on single-waveguide-coupled microring resonators using SU8 and silicon-on-insulator (SOI) platforms, respectively.

Previously, our research group demonstrated micron-sized polystyrene particle buffering and dropping on dual-waveguide-coupled microring- and microdisk-resonator-based add-drop devices using silicon nitride (SiN)-on-silica platform^{10, 11, 17}. Our demonstrated microresonator-based add-drop devices enable particle buffering inside the microresonator for multiple round-trips upon a sharp optical resonance with a relatively high quality (Q) factor, and particle routing to the drop-waveguide (particle dropping) upon a relatively low- Q optical resonance. We attributed the particle buffering to a sufficiently large intensity build-up in the microresonator at high- Q resonances, and the particle dropping to a relatively weak intensity build-up in the microresonator at low- Q resonances.

However, it has not been entirely clear what the detailed criterion is in terms of the Q factor for determining particle buffering or dropping at an on-resonance state, or whether the particle transport processes at cavity resonances are deterministic or probabilistic.

Photonic Device Laboratory, Department of Electronic and Computer Engineering, The Hong Kong University of Science and Technology, Clear Water Bay, Hong Kong SAR, China. E-mail: eeawpoon@ust.hk; Fax: 852 2358 1485; Tel: 852 2358 8532

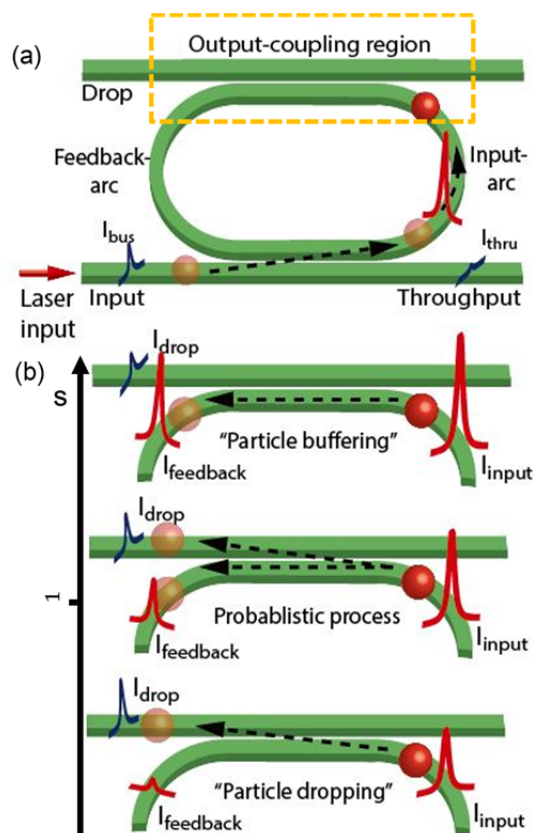


Fig. 1 (a) Schematic of microparticle transport processes on a microring-resonator-based add-drop device on an optofluidic chip. A particle is trapped and transported from the input-waveguide to the microring input-arc at an on-resonance wavelength. (b) The relationship between particle transport processes in the output-coupling region at on-resonance wavelengths and the S factor. From top to bottom: (1) Deterministic particle buffering with S sufficiently exceeding 1 (I_{feedback} is sufficiently exceeding I_{drop}). (2) Probabilistic particle transport processes with S comparable to 1 (I_{feedback} is comparable to I_{drop}). (3) Deterministic particle dropping with S sufficiently below 1 (I_{feedback} is sufficiently below I_{drop}).

In this paper, we address the above by proposing an intuitive and quantitative design rule that determines particle buffering and dropping in microring-resonator-based add-drop devices at cavity resonances. Our experimental studies reveal that we can realize deterministic particle buffering and dropping by properly tailoring the splitting ratio, S , of the optical-field intensity of the microring feedback-arc just after the output-coupling region to that of the drop-waveguide. We also realize switching between deterministic particle buffering and probabilistic particle transport processes on a single add-drop device based on tuning the S factor upon different polarization modes.

Principles

Fig. 1 schematically depicts the working principles of particle transport on a microring resonator-based add-drop device. The steady-state guided-field intensity distribution determines the particle transport process. At microring off-resonance wavelengths, the intensity along the microring input-arc (I_{input})

is lower than that remained in the input-waveguide toward the throughput-port (I_{thru}), and thus the particle remains guided in the input-waveguide propagating toward the throughput-port. This is known as “particle throughput.” At microring on-resonance wavelengths, I_{input} exceeds I_{thru} . Thus, a particle that is trapped and guided by the input-waveguide toward the waveguide-microring input-coupling region is coupled to the microring, and subsequently guided along the microring input-arc, as shown in Fig. 1(a).

The particle guided on the microring has two possible particle transport processes. The particle can be buffered on the microring for round trips upon a relatively high- Q resonance (until the particle randomly escapes or gets stuck on the microring surfaces due to particle-surface interaction), or it can be routed to the drop-port without completing round trips upon a relatively low- Q resonance. The former is known as “particle buffering.” The latter is referred to as “particle dropping.” The problem is what physical criterion determines the particle transport processes at cavity resonances.

Based on our previous work¹⁰, it is the steady-state difference between the intensity in microring feedback-arc (I_{feedback}) and the intensity coupled to the drop-waveguide towards the drop-port (I_{drop}), both determined right after the output-coupling region, that determines particle buffering or dropping. Upon a relatively high- Q resonance, $I_{\text{feedback}} > I_{\text{drop}}$, the particle is routed to the microring feedback-arc and buffered. Upon a relatively low- Q resonance, I_{drop} either exceeds or is comparable to I_{feedback} , the particle is then either dropped or the particle transport process becomes random.

Here, we define the intensity ratio, $S \equiv I_{\text{feedback}} / I_{\text{drop}}$, as a figure-of-merit for particle transport on microring-resonator-based add-drop devices at cavity resonances. Following the above discussion, $S > 1$ suggests deterministic particle buffering, while $S < 1$ suggests deterministic particle dropping. In the case that $S \approx 1$, the particle transport process is random. Fig. 1(b) schematically depicts the proposed criterion.

According to transfer-matrix modelling¹⁸, and assuming lossless identical coupling between the microring and the two bus waveguides in an add-drop device configuration, we express S as follows:

$$S \equiv \frac{I_{\text{feedback}}}{I_{\text{drop}}} = \frac{1 - |\kappa_2|^2}{|\kappa_2|^2} \quad (1)$$

where κ_2 is the complex field-amplitude output-coupling coefficient. According to eqn (1), we can tailor S by varying κ_2 through designing the waveguide-to-microring interaction length (L_c), the coupling gap spacing, the effective refractive index (n_{eff}) and the waveguide dimensions of the bus waveguides and the microring. In the following, we experimentally investigate the validity of the proposed criterion or design rule by studying particle buffering and dropping on various fabricated devices upon different extracted S values. We show that the S value provides a more transparent guideline to determine particle transport processes at cavity resonances than the Q factor does.

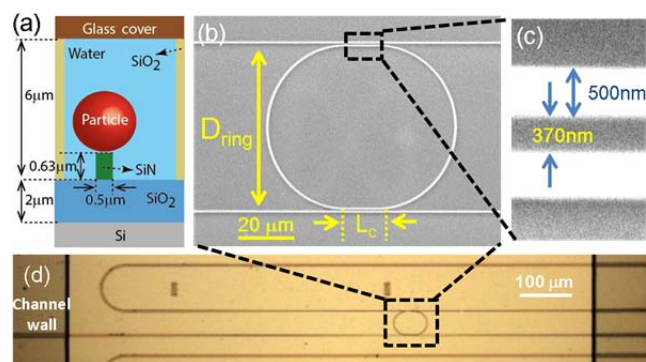


Fig. 2 (a) Schematic cross-sectional view of the optofluidic chip with a trapped microparticle. (b) Top-view SEM image of the fabricated microring-resonator-based add-drop device. D_{ring} : arc diameter, L_c : interaction length. (c) Zoom-in-view SEM image of the coupling gap. (d) Top-view optical micrograph of the fabricated optofluidic chip with air-cladding.

Testing the proposed design rule

A. Device design and fabrication

In order to test the proposed design rule, we design and fabricate the add-drop devices on a SiN-on-silica substrate integrated with microfluidic channels. Fig. 2(a) schematically shows the cross-sectional view of the optofluidic chip. The SiN device layer of $0.63\mu\text{m}$ -thick is prepared by low-pressure chemical vapour deposition (LPCVD) on a $2\mu\text{m}$ -thick SiO_2 under-cladding layer on a $4''$ silicon wafer. We transfer the device pattern onto the substrate using i-line (365 nm) photolithography and reactive ion etching. We form the microfluidic channel encompassing the microring devices using a $6\mu\text{m}$ -height silica layer patterned on top of the SiN layer by i-line photolithography and wet etching. The fluidic channel is covered by a cover-glass.

We design the racetrack microrings with two different arc diameters ($D_{\text{ring}} = 30, 50\mu\text{m}$) and three different interaction lengths ($L_c = 10, 15, 30\mu\text{m}$). The designed waveguide width and height are 500 nm and 630 nm, respectively. The fabricated coupling gap spacing is ~ 370 nm. Figs. 2(b) and (c) show the scanning electron microscope (SEM) top-view image of one fabricated add-drop device and a zoom-in view of its coupling gap. Fig. 2(d) shows the top-view optical micrograph of the fabricated optofluidic chip.

B. Optical transmission characterization

We first characterize the optical transmission characteristics of the microring devices covered by deionized (DI) water cladding without particles. We end-fire $\sim 100\text{mW}$ transverse-magnetic (TM)-polarized (E-field \perp chip) wavelength-tunable laser light at $1.55\mu\text{m}$ into a $\sim 4\mu\text{m}$ -wide tapered waveguide using a polarization-maintaining singlemode lensed fiber with a spot diameter of $\sim 2.5\mu\text{m}$. The laser light is amplified by an erbium-doped fiber amplifier (EDFA).

Figs. 3(a)-(d) show the measured throughput- and drop-transmission spectra around a resonance of devices A, B, C and D of different D_{ring} and L_c values. The four devices under test are on four separate chips diced from the same wafer. The

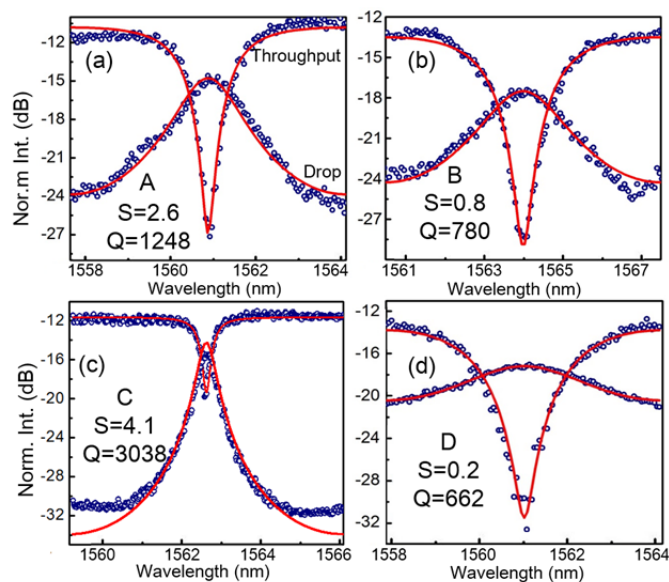


Fig. 3 (a)-(d) Measured and fitted throughput- and drop-transmission spectra of (a) A, (b) B, (c) C and (d) D. Blue circles: data. Red lines: fitting according to transfer-matrix modelling.

Table 1 Device design parameters of A - D and their corresponding resonance wavelengths, measured Q factor values, fitted κ_2 and S values.

	A	B	C	D
D_{ring} (μm)	30	50	50	50
L_c (μm)	15	10	15	30
Resonance Wavelength (nm)	1560.9	1563.9	1562.5	1561.1
Q factor	1248	780	3038	662
κ_2	0.53	0.74	0.44	0.91
S factor	2.6	0.8	4.1	0.2

transmission intensities are normalized to the output intensity from the lensed fiber. The measured transmission spectra reveal for each device a total insertion loss of $\sim 12 - 13$ dB at an off-resonance wavelength. We attribute ~ 7 dB loss partly to the mode-area mismatch between the lensed fiber and the tapered waveguide, and partly to the waveguide end-face reflection. We attribute $\sim 5 - 6$ dB loss to a relatively large waveguide propagation loss along a waveguide length of ~ 6 mm (a waveguide propagation loss of ~ 1 dB/mm). We thus estimate the guided power as $\sim 10 - 11.2$ mW at the input-waveguide by the microring, which is ~ 3 mm away from the input-waveguide end-face.

The transmission spectra reveal a resonance Q factor of 1248 for A, 780 for B, 3038 for C and 662 for D. In order to extract the S factor using eqn (1), we fit both the throughput- and drop-transmission spectra using transfer-matrix modelling¹⁸. We extract the S factor of 2.6 for A, 0.8 for B, 4.1 for C and 0.2 for D. Table 1 summarizes the device design parameters and their corresponding resonance wavelengths, Q factor, fitted κ_2 and S factor values.

C. Particle trapping experiments

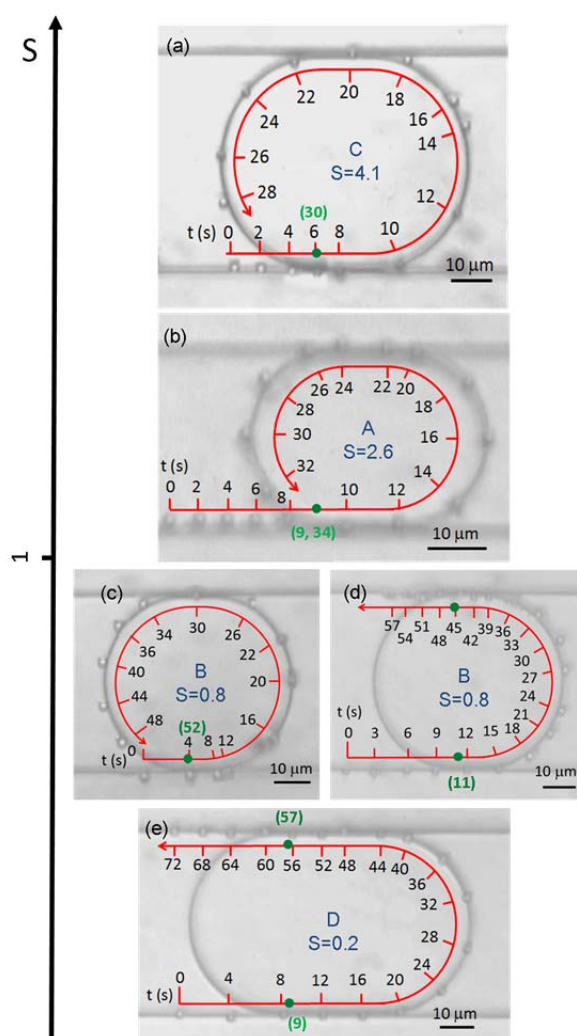


Fig. 4 (a)-(e) Composite bright-field images of a single optically manipulated $2.2\mu\text{m}$ microparticle upon the TM polarization. The time axes indicate the duration of the particle manipulation. (a) Deterministic particle buffering on C. (b) Deterministic particle buffering on A. (c), (d) Probabilistic particle buffering and dropping on B. (e) Deterministic particle dropping on D. Green dots: starting and ending positions for determining the buffering round-trip time or the time for dropping the particle.

For particle trapping experiments, we inject a diluted colloidal solution of $2.2\mu\text{m}$ or $0.84\mu\text{m}$ polystyrene particles (Spherotech, $\pm 2.5\%$ size distribution, concentration of $\sim 2 \times 10^8$ particles/ml) into the microfluidic channel. We choose the particle concentration in order to observe on average one particle per minute randomly diffused into the device area, as viewed by the top-view microscope. The fluidic medium remains essentially static shortly after filling up the microfluidic channel and during the entire duration of the experiment. Each experiment lasts ~ 20 min until the water evaporation results in a partially unfilled and unstable microfluidic channel.

For the particle trapping experiments with the estimated guided power reduced to below 8 mW, we fail to observe steady particle trapping and transport. With the estimated guided power exceeds 28 mW, however, most of the particles end up sticking at the waveguide surfaces and lined up along the input-waveguide. We therefore fix the estimated guided

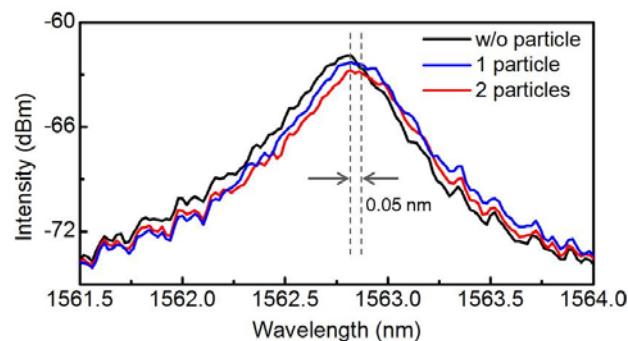


Fig. 5 Measured drop-port transmission spectra of C upon zero, one and two trapped $2.2\mu\text{m}$ particles.

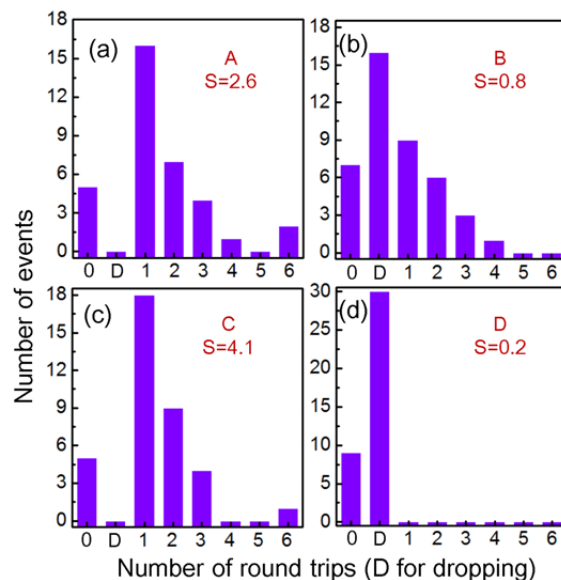


Fig. 6 (a)-(d) Summary of $2.2\mu\text{m}$ particle transport processes on A - D at on-resonance wavelengths. All particles are routed from the input-waveguide. The "0" bin: particle escaping without completing one round trip. The "D" bin: particle dropping.

power around 10 - 11.2 mW for the particle trapping experiments.

We monitor the particle transport events using a top-view imaging system with a long-working-distance microscope composite single-particle transport trajectories of $2.2\mu\text{m}$ particles on A, B, C and D at their corresponding resonance wavelengths. All particles studied are routed from the input-waveguide. The particles are typically guided on the top surface of the waveguide, as expected from the TM mode-field profile that exhibits a larger field-amplitude along the waveguide top surface than along the waveguide sidewalls.

For C and A with the extracted S values > 1 , we observe particle buffering (Figs. 4(a) and (b)). The particle round-trip time on C is ~ 24 s (from time $t \approx 6$ s to $t \approx 30$ s), and that on A is ~ 25 s (from $t \approx 9$ s to $t \approx 34$ s). We note that C has a longer microring round-trip length than A (see Table 1), and thus the buffered particle travels faster on C.

For B with the extracted S value close to 1, we observe either particle buffering or dropping (Figs. 4(c) and (d)). The particle round-trip time is ~ 48 s (from $t \approx 4$ s to $t \approx 52$ s). The time for

the dropped particle to route from the input-waveguide to the drop-waveguide is ~ 34 s (from $t \approx 11$ s to $t \approx 45$ s).

For D with the extracted S value < 1 , we observe particle dropping (Figs. 4(e)). The time for the particle to route from the input-waveguide to the drop-waveguide is ~ 48 s (from $t \approx 9$ s to $t \approx 57$ s).

We confirm that the microring resonance is not significantly perturbed in the presence of one to two trapped particles. In order to monitor the perturbation to the microring resonances while trapping particles, we use an EDFA seeded by a laser light at a fixed wavelength as a low-coherence light source and measure the transmission spectra using an optical spectrum analyser (OSA).

Fig. 5 shows the measured drop-port transmission spectra of C upon zero, one and two trapped $2.2\mu\text{m}$ particles. Upon trapping two particles, we observe the resonance wavelength redshifts by ~ 0.05 nm, which is within the resonance linewidth, and the peak intensity drops by ~ 1 dB. Thus, the microring resonance is not significantly perturbed upon trapping single particles.

For each device, we repeat the $2.2\mu\text{m}$ particle trapping experiments for a total of ~ 300 min (~ 15 runs). Although in general we observe one particle event per minute, most of the particles pass through the device from random directions slightly above the device without interacting with the surface field. On average only approximately 10% of the observed single-particle events result in particle trapping and guiding by the input-coupled waveguide.

In between runs, we rinse the chip by injecting DI water to remove any particles attached to the device. Once the rinse fails to remove an attached particle, we employ ultrasonic cleaning in acetone for ~ 5 min, followed by isopropyl alcohol (IPA), rinsed with DI water and dried with a nitrogen flow. However, the chip performance tends to degrade after a couple rounds of ultrasonic cleaning (which tends to cause erosion to the chip). This practically limits the chip lifetime to ~ 15 experimental runs and thus the statistics of single-particle events accumulated for each device.

Figs. 6(a)-(d) summarize our accumulated statistics of $2.2\mu\text{m}$ particle transport processes on the four different devices. For A, we study a total number of 35 single-particle events, with 30 particles buffered for one or multiple round trips, 0 particles dropped and 5 particles randomly escaped without completing one round trip (Fig. 6(a)). The average number of buffering round trips is 1.7. The buffered particles typically end up being attached on the microring sidewalls while the laser light is on, and detached upon switching off the laser light. Some buffered particles randomly escape from the microring into the fluidic medium.

For B, we study a total number of 42 single-particle events, with 19 particles buffered for one or multiple round trips, 16 particles dropped and 7 particles randomly escaped without completing one round trip (Fig. 6(b)). The average number of buffering round trips is 0.8. For C, we study a total number of 37 single-particle events, with 32 particles buffered for one or multiple round trips, 0 particles dropped and 5 particles

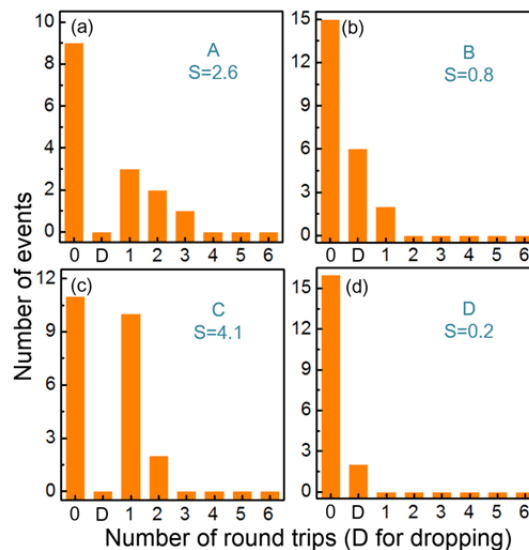


Fig. 7 (a)-(d) Summary of $0.84\mu\text{m}$ particle transport processes on A - D at on-resonance wavelengths. All particles are routed from the input-waveguide. The "0" bin: particle escaping without completing one round trip. The "D" bin: particle dropping.

randomly escaped without completing one round trip (Fig. 6(c)). The average number of buffering round trips is 1.3. We note that the average number of buffering round trips for C is smaller than that for A. We attribute this to the longer round-trip length for C (see Table 1).

For D, we study a total number of 39 single-particle events, with 0 particles buffered, 30 particles dropped and 9 particles randomly escaped without completing one round trip (Fig. 6(d)).

After the $2.2\mu\text{m}$ particle trapping experiments, we further test the proposed design rule using $0.84\mu\text{m}$ particles on the same four devices. The total experimental time for each device is shortened to ~ 100 min till the device becomes obviously degraded.

Figs. 7(a)-(d) summarize our accumulated statistics of particle transport processes of $0.84\mu\text{m}$ particles on A - D. For all devices, we observe much more random particle escape events compared with $2.2\mu\text{m}$ particles. We attribute this to the reduced optical gradient force due to the reduced particle size.

For A, we observe a total number of 15 single-particle events, with 6 particles buffered for one or multiple round-trips, 0 particles dropped and 9 particles randomly escaped without completing one round trip (Fig. 7(a)). The average number of buffering round-trips is 0.7.

For B, we observe a total number of 23 single-particle events, with 2 particles buffered for one round trip, 6 particles dropped and 15 particles randomly escaped without completing one round-trip (Fig. 7(b)). The average number of buffering round-trips is 0.1.

For C, we observe a total number of 23 single-particle events, with 12 particles buffered for one or multiple round trips, 0 particles dropped and 11 particles randomly escaped without completing one round-trip (Fig. 7(c)). The average number of buffering round-trips is 0.6.

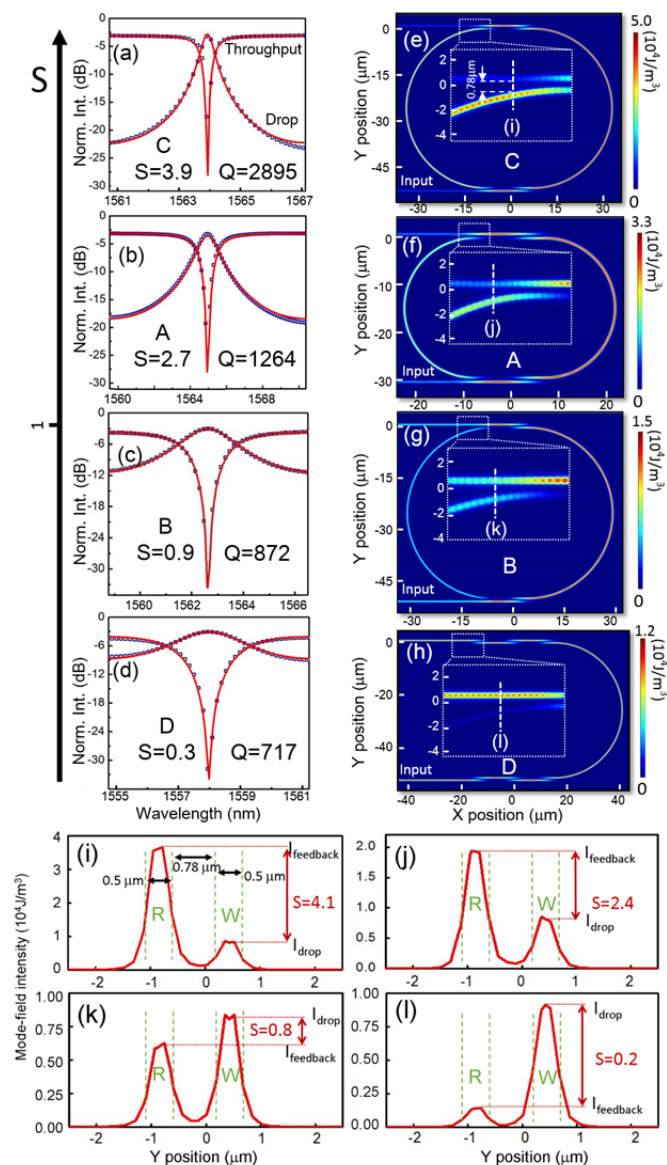


Fig. 8 (a)-(d) Simulated throughput- and drop-transmission spectra of (a) C, (b) A, (c) B and (d) D. Blue squares: simulated data; Red curves: fitting according to transfer-matrix modelling. (e)-(h) Corresponding mode-field intensity distributions at on-resonance wavelengths and zoom-in views on the output-side of the output-coupling regions for (e) C, (f) A, (g) B and (h) D. (i)-(l) Mode-field intensity profiles in the y direction at the output-end of the output-coupling regions along the dashed lines (i)-(l) in (e)-(h) for (i) C, (j) A, (k) B and (l) D.

For D, we study a total number of 18 single-particle events, with 0 particles buffered, 2 particles dropped and 16 particles randomly escaped without completing one round-trip (Fig. 7(d)).

Our experimental results on both $2.2\mu\text{m}$ and $0.84\mu\text{m}$ particle trapping are consistent with the proposed design rule. Only the average numbers of buffering round trips reduce with particle size. Our accumulated statistics therefore support the proposed design rule, revealing that $S > 1$ (A and C) gives deterministic particle buffering, $S < 1$ (D) gives deterministic particle dropping, while $S \approx 1$ (B) gives probabilistic particle transport. Given the same statistics, it is however difficult to see a clear physical criterion in terms of the Q factor.

Table 2 Device design parameters of devices A - D and their corresponding resonance wavelengths, Q factor values, fitted κ_2 and S values from simulated spectra and extracted S values from mode-field profiles.

	A	B	C	D
D_{ring} (μm)	30	50	50	50
L_c (μm)	15	10	15	30
Resonance Wavelength (nm)	1565.0	1562.6	1563.9	1558.0
Q factor	1264	872	2895	717
κ_2	0.52	0.73	0.45	0.88
S factor (fitting)	2.7	0.9	3.9	0.3
S factor (profile)	2.4	0.8	4.1	0.2

Visualising the S factor from simulations

In order to visualize the S factor and correlate the extracted S factor values from transmission spectra to the corresponding mode-field intensity distributions, we numerically simulate the four devices following their design parameters using finite-element method (FEM) (COMSOL RF module). Limited by our computation power, we adopt only two-dimensional (2D) modelling. In order to account for the vertical dimension, we set the effective refractive index contrast between the SiN and the surrounding medium (water upper-cladding and silica lower-cladding) as 1.81:1.39, according to beam-propagation method. We assume the waveguide mode is in the TM polarization.

Figs. 8(a)-(d) show the simulated normalized throughput and drop-port transmission spectra (in squares) for the four devices. We normalize the simulated transmission spectra to a waveguide input power of 1 W. We fit both the throughput and drop-transmission spectra according to the transfer-matrix modelling¹⁸. The extracted S factor values from the fitted spectra for C, A, B and D are 3.9, 2.7, 0.9 and 0.3, respectively. The S factor values are consistent with those extracted from the experiments (see Fig. 3).

Figs. 8(e)-(h) show the simulated mode-field intensity distributions at the corresponding resonance wavelengths of the four devices. Insets show the zoom-in views of the mode-field intensity profiles on the output-side of the output-coupling regions. We define the output-coupling region as where the coupling gap spacing between the microring and the drop-waveguide is narrower than half the wavelength ($\sim 0.78\mu\text{m}$). We define the origin of the x - y coordinates in the middle of the coupling gap at the center of the output-coupling region. The dashed lines (i)-(l) in the transverse y direction indicate the positions where the coupling gap spacing is $0.78\mu\text{m}$. Figs. 8(i)-(l) show the mode-field intensity profiles along the dashed lines. We extract the I_{drop} and the I_{feedback} as the peak intensities within the drop-waveguide (W) and microring (R) regions, respectively. The extracted S factor values from the mode-field intensity distributions for C, A, B and D are 4.1, 2.4, 0.8 and 0.2, respectively. These S factor values are consistent with those extracted from the simulated transmission spectra (Figs. 8(a)-(d)). Table 2 summarizes for the four simulated devices

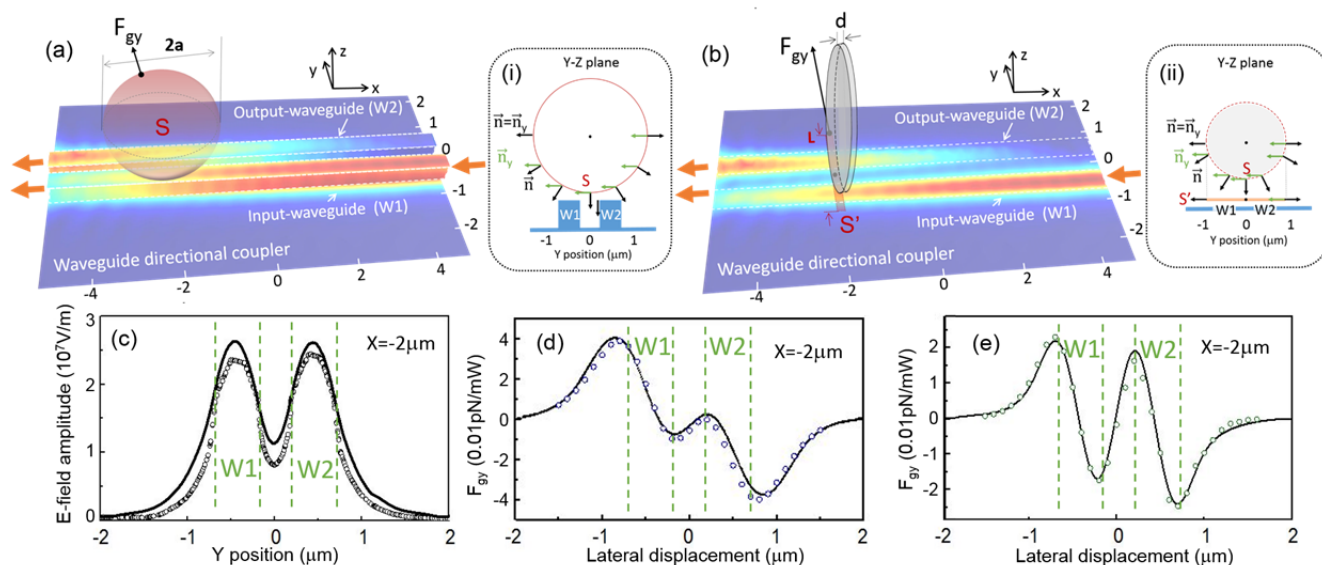


Fig. 9 (a) Schematic of the 3D model for optical force field calculations, with the 3D-FEM-simulated mode-field-amplitude profile of the waveguide coupler. Inset (i): Cross-sectional-view schematic of the 3D model in the y - z plane. (b) Schematic of the effective microdisk model, with the 2D-FEM-simulated mode-field-amplitude profile of the waveguide coupler. Inset (ii): Cross-sectional-view schematic of the effective microdisk model in the y - z plane. (c) Calculated input-normalized profiles at $x = -2 \mu\text{m}$ for the evanescent field amplitude profile at 30nm above the waveguide top surface in the 3D model and the waveguide mode-field amplitude in the 2D model. (d)-(e) Calculated F_{gy} at $x = -2 \mu\text{m}$ at different lateral displacements based on the 3D model and the effective microdisk model for (d) $2.2\mu\text{m}$ particles and (e) $0.84\mu\text{m}$ particles. Circles: 3D model. Solid lines: effective microdisk model.

the corresponding resonance wavelengths, Q factor, fitted κ_2 , S factor values extracted by spectra fitting and S factor values extracted from the simulated model-field distributions.

Numerical simulation of optical force fields

In order to better explain the particle transport processes on a microring-resonator-based add-drop device at cavity resonances, we numerically calculate the optical force field magnitude, F , exerted on a microparticle by the evanescent field of the waveguide mode using the Maxwell stress tensor as follows^{6, 19}:

$$F(\mathbf{r}) = \oint_S \bar{\mathbf{T}} \cdot \mathbf{n} dS \quad (2)$$

where $\bar{\mathbf{T}}$ is the Maxwell stress tensor and \mathbf{n} is the unit normal vector pointing outward from the microparticle surface, S , and \mathbf{r} is the position vector of the microparticle. We define \mathbf{r} relative to an origin of the coordinate axes positioned at the center of the output-coupling region, with the $z = 0$ plane at the interface between the waveguide core and the under-cladding. We only analyze the optical gradient force component exerted on the microsphere in the y direction, F_{gy} , which determines the particle transport processes between the microring and the drop-waveguide.

For a homogeneous, non-elastic, dielectric microsphere with a refractive index n_2 immersed in a surrounding isotropic medium of a refractive index n_1 , we can simplify eqn (2) to calculate F_{gy} , as follow:

$$F_{gy}(\mathbf{r}) = \frac{1}{2} \epsilon_0 \oint_S |E|^2 (n_2^2 - n_1^2) \mathbf{n}_y \cdot \mathbf{n} dS \quad (3)$$

where ϵ_0 is the free-space permittivity and E is the complex optical field amplitude of the evanescent field of the waveguide

mode, \mathbf{n}_y is the unit vector in the y direction. In our calculations, we adopt $n_2 = 1.55$ for polystyrene and $n_1 = 1.33$ for water.

Fig. 9(a) shows in perspective view the schematic for calculating the optical force field exerted on a microsphere by a waveguide directional coupler. Inset (i) shows in the y - z plane the vector relationship and the surface integral involved in the model. We assume a microsphere with a radius of a is located at a distance of 30nm above the top surface of a waveguide directional coupler (assuming a Debye length of 30nm ²⁰). The coupler follows our device design parameters in order to numerically model a section of the output-coupling region using three-dimensional (3D) FEM. We calculate the TM-polarized E-field distribution of the coupler in the presence of the microsphere. This enables us to calculate from eqn (3) the F_{gy} exerted on the microsphere by the evanescent field of the coupler.

However, limited by our computation power, it is not practical to numerically study in 3D simulations the microparticle transport processes on relatively large-sized microring add-drop devices. Instead, we approximate the 3D calculation by using an effective microdisk model.

Fig. 9(b) shows in perspective view the schematic of the microdisk model. Inset (i) shows in the y - z plane the vector relationship and the surface integral involved in the model. The microparticle is modeled as a homogeneous, non-elastic, dielectric microdisk of refractive index n_2 with a radius of a and a thickness of d . The microdisk plane is in the y - z plane perpendicular to the waveguide direction. Such a microdisk models a thin circular disk centered at the microsphere. The effective integration surface, S , is then given by the microdisk edge surface, with \mathbf{n} in the y - z plane. We assume the

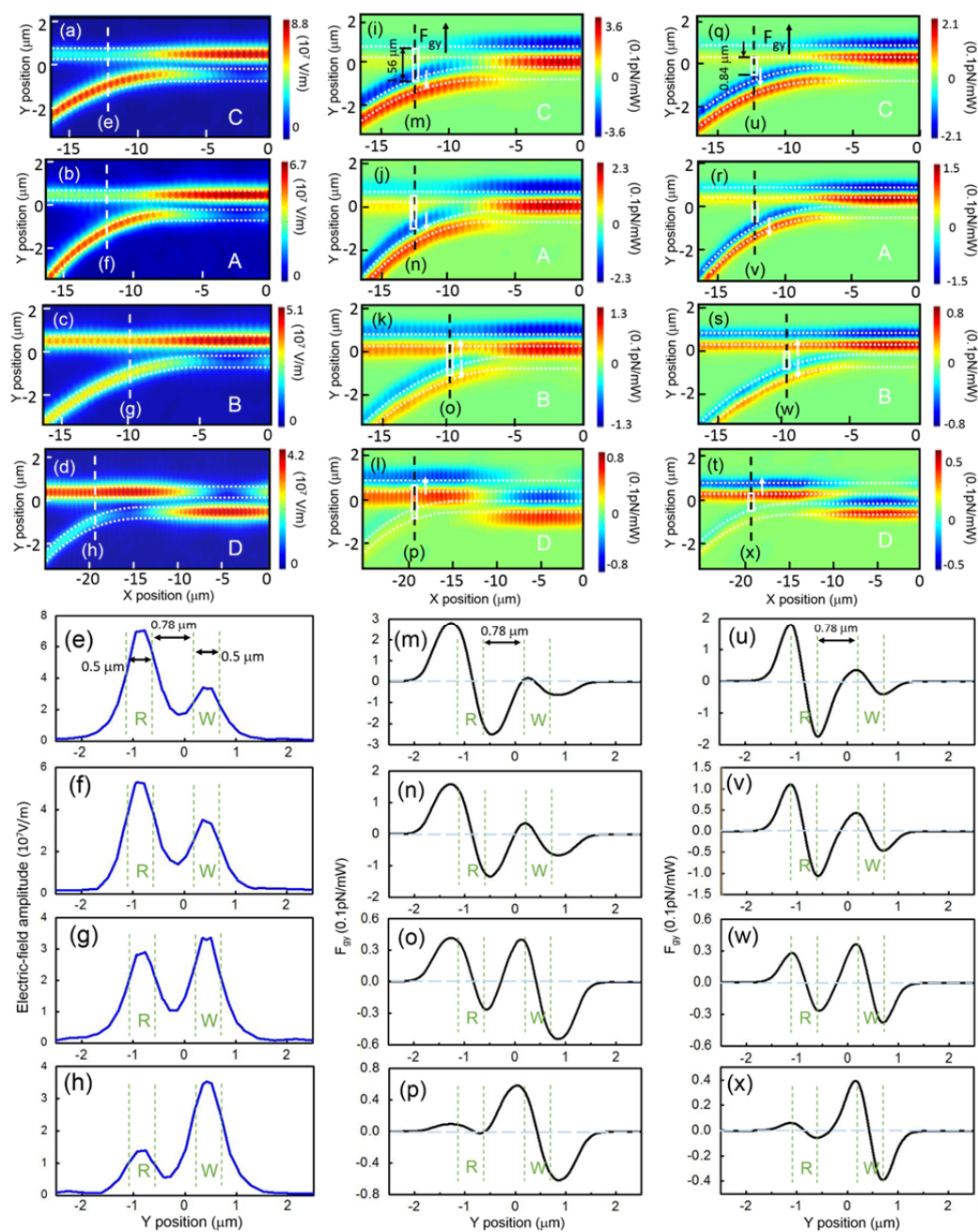


Fig. 10 (a)-(d) Simulated mode-field-amplitude distributions on the output-side of the output-coupling regions of (a) C, (b) A, (c) B and (d) D. (e)-(h) Mode-field amplitude profiles in the y direction along the dashed-lines (e) – (h) in (a) – (d) of (e) C, (f) A, (g) B and (h) D. (i)-(l) F_{gy} distributions exerted on the modeled $2.2\mu\text{m}$ microparticle on the output-side of the output-coupling regions of (i) C, (j) A, (k) B and (l) D. (m)-(p): F_{gy} profiles on the modeled $2.2\mu\text{m}$ microparticle in the y direction along the dashed-lines (m) – (p) in (i) – (l) of (m) C, (n) A, (o) B and (p) D. (q)-(t) F_{gy} distributions exerted on the modeled $0.84\mu\text{m}$ microparticle on the output-side of the output-coupling regions of (q) C, (r) A, (s) B and (t) D. (u)-(x): F_{gy} profiles on the modeled $0.84\mu\text{m}$ microparticle in the y direction along the dashed-lines (u) – (x) in (q) – (t) of (u) C, (v) A, (w) B and (x) D. White rectangles: the microparticle.

microdisk-induced perturbation to the waveguide mode-field distribution is negligible. We then calculate the TM-polarized E-field distribution of the coupler in the absence of the microdisk using waveguide evanescent field amplitude. We then calculate F_{gy} exerted on the microdisk by the waveguide mode field using eqn (3) by integrating the lateral optical force density across an only 2D FEM. Such a calculation, however, does not yield the effective projected microdisk edge surface, S' , on the x - y plane.

S' has a length of $l \leq 2R$ in the y direction and a width of d in the x direction. We choose l and d by matching the calculated F_{gy} values from the effective microdisk model with those obtained from the 3D model.

We first evaluate the simulated electric-field amplitude profiles of the waveguide coupler in the y direction (normalized to the waveguide input-power of 1 W) using the 3D FEM in the presence of the microsphere and the 2D FEM in the absence of the microdisk. Fig. 9(c) shows the calculated electric-field

amplitude profiles at $x = -2 \mu\text{m}$ for the evanescent field at 30nm above the waveguide top surface in the 3D model and for the waveguide mode field in the 2D model. Both the calculated field amplitude profiles reveal two Gaussian-like field distributions, with nearly equal peak amplitudes in the input-waveguide (W1) and output-waveguide (W2) regions.

We compare the resulting F_{gy} values exerted on $2.2\mu\text{m}$ and $0.84\mu\text{m}$ particles at $x = -2 \mu\text{m}$ by the waveguide coupler using the 3D model and the effective microdisk model. We assume a lateral displacement step of $0.1 \mu\text{m}$ in the microsphere model and of $0.01 \mu\text{m}$ in the effective microdisk model. By matching the calculated F_{gy} values from the effective microdisk model with those of the 3D model, we find a good agreement by adopting $d = 0.1 \mu\text{m}$, with $l = 1.56 \mu\text{m}$ to model a $2.2\mu\text{m}$ microsphere and $l = 0.84 \mu\text{m}$ to model a $0.84\mu\text{m}$ microsphere, as shown in Figs. 9(d)-(e).

Hence, in the following analysis of the particle add-drop device configurations, we adopt the effective microdisk model with the d and l values above. We assume the calculated mode-field distributions in Figs. 8(e)-(h).

Figs. 10(a)-(d) show the calculated mode-field distributions on the output-side of the output-coupling regions of C, A, B and D. Figs. 10(e)-(h) show the mode-field amplitude profiles in the y direction at the same x positions where the S factors are extracted in Figs. 8(e)-(h). The calculated profiles reveal two Gaussian-like field distributions, with peak amplitudes near the waveguide axis in the microring (R) and drop-waveguide (W) regions.

Figs. 10(i)-(l) show the resulting F_{gy} distributions exerted on the modeled $2.2\mu\text{m}$ microparticle on C, A, B and D. Figs. 10(m)-(p) show the F_{gy} profiles in the y direction, given by the mode-field amplitude profiles shown in Figs. 10(e)-(h), respectively.

Within the microring and drop-waveguide regions, a negative slope in F_{gy} over the y position, with F_{gy} crossing zero, suggests a restoring force to trap the particle along the waveguide axis of both the microring feedback-arc and the drop-waveguide. Whereas, in the coupling gap region, a positive slope in F_{gy} over the y position indicates different particle transport processes depending on the sign of F_{gy} .

For $S > 1$ in C and A, the microring region exhibits a larger restoring force (a steeper slope in F_{gy}) than the drop-waveguide region. While, the coupling gap region exhibiting a negative F_{gy} suggests an increasing force pulling the particle toward the microring (Figs. 10(m) and (n)). Thus, C and A enable deterministic particle buffering.

For $S < 1$ in D, the drop-waveguide region exhibits a larger restoring force than the microring region. While, the coupling gap region exhibiting a positive F_{gy} suggests an increasing force pulling the particle toward the drop-waveguide (Fig. 10(p)). Thus, D enables deterministic particle dropping.

For $S \approx 1$ in B, the microring and drop-waveguide regions exhibit comparable restoring force. While, the coupling gap region exhibiting a F_{gy} crossing zero suggests an increasing force pulling the particle either toward the microring or the

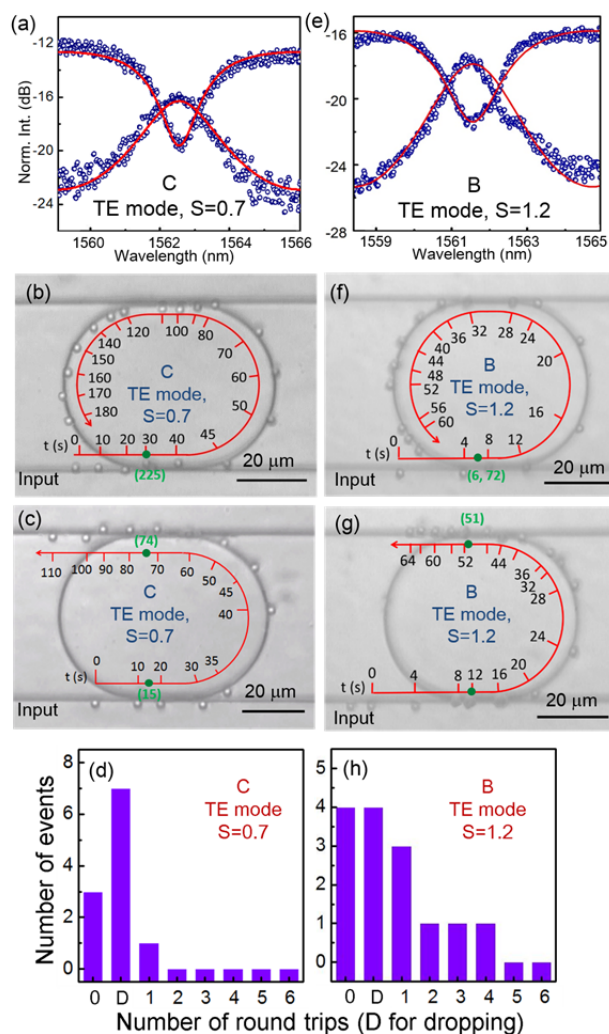


Fig. 11 (a), (e) Measured and fitted throughput- and drop-transmission spectra of (a) C and (e) B upon the TE polarization. Blue circles: data; Red curves: fitting according to transfer-matrix modelling. (b)-(c) Composite bright-field images of a single optically manipulated $2.2\mu\text{m}$ microparticle on C. (b) Probabilistic particle buffering. (c) Probabilistic particle dropping. (f)-(g) Composite bright-field images of a single optically manipulated $2.2\mu\text{m}$ microparticle on B. (f) Particle buffering. (g) Particle dropping. The time axes indicate the duration of the optical manipulation. Green dots: starting and ending positions of the particle for determining buffering round-trip time or the time for dropping the particle. (d), (h) Summary of particle transport processes on C and B in the TE mode at on-resonance wavelengths. All particles are routed from the input-waveguide. The "0" bin: particle escaping without completing one round trip. The "D" bin: particle dropping.

drop-waveguide (Fig. 10(o)). Thus, B exhibits probabilistic particle transport processes.

Likewise, Figs. 10(q)-(t) show the resulting F_{gy} distributions exerted on the modeled $0.84\mu\text{m}$ microparticle on C, A, B and D. Figs. 10(u)-(x) show the F_{gy} profiles in the y direction, given by the mode-field amplitude profiles shown in Figs. 10(e)-(h), respectively. The F_{gy} exerted on the $0.84\mu\text{m}$ particle is generally smaller than that exerted on the $2.2\mu\text{m}$ particle. The F_{gy} distributions for the two particle sizes are otherwise largely similar and show the same dependence on the S factor.

Tuning the S factor

Based on our recent work²¹, we further test the proposed design rule on C and B using 2.2 μm particles by tuning the S factor upon different polarization modes.

Fig. 11(a) shows the measured and fitted throughput- and drop-port transmission spectra from C (with DI water cladding) upon the transverse-electric (TE) polarization (E-field // chip). Given the $\sim 13\text{dB}$ insertion loss at off-resonance wavelengths and a launched optical power of $\sim 100\text{ mW}$, the estimated guided power at the input-waveguide by the microring is $\sim 10.0\text{ mW}$. The measured Q factor is ~ 658 at a resonance wavelength of $\sim 1562.5\text{ nm}$ (accidentally degenerate with the TM-mode resonance). The extracted S factor is ~ 0.7 , which is a significant tuning from ~ 4.1 in the TM mode. According to the proposed design rule, we expect C in the TE mode to exhibit probabilistic particle transport processes.

Figs. 11(b)-(c) show the representative composite trajectories of single 2.2 μm particle buffering and dropping on C upon the TE polarization. The particle round-trip time is $\sim 195\text{ s}$ (from $t \approx 30\text{ s}$ to $t \approx 225\text{ s}$). The time for the particle to route from the input-waveguide to the drop-waveguide is $\sim 59\text{ s}$ (from $t \approx 15\text{ s}$ to $t \approx 74\text{ s}$). We observe a total of 11 single-particle events for a total of $\sim 100\text{ min}$, with 1 particle buffered for one round trip, 7 particles dropped and 3 particles escaped without completing one round trip (Fig. 11(d)). We note that the particles are always guided along the waveguide sidewalls. This agrees with the TE mode-field profile, with a larger field-amplitude along the waveguide sidewalls than along the waveguide top surface.

For B, the measured Q is ~ 1062 at a resonance wavelength of $\sim 1561.6\text{ nm}$ in the TE mode. The extracted S factor is ~ 1.2 , which does not vary a lot from ~ 0.8 in the TM mode. We therefore expect B in the TE mode to again exhibit probabilistic particle transport processes. Polarization mode tuning in this case is not effective in tuning the S factor.

Figs. 11(f)-(g) show the representative composite trajectories of single 2.2 μm particle buffering and dropping on B upon the TE polarization. The particle round-trip time is $\sim 66\text{ s}$ (from $t \approx 6\text{ s}$ to $t \approx 72\text{ s}$). The time for the particle to route from the input-waveguide to the drop-waveguide is $\sim 39\text{ s}$ (from $t \approx 12\text{ s}$ to $t \approx 51\text{ s}$). We observe a total of 14 single-particle events for a total of $\sim 100\text{ min}$, with 4 particles buffered for one round trip, 6 particles dropped and 4 particles escaped without completing one round trip (Fig. 11(h)).

We remark that in order to attain an effective tuning of S factor through switching polarization modes, it should be critical to carefully design a large difference of S factors between the TE and TM modes.

Conclusions

In summary, we proposed and experimentally examined a design rule for deterministic particle buffering and dropping on microring-resonator-based add-drop devices at cavity resonances. We defined the splitting ratio, S, of the optical-field intensity at the microring feedback-arc just after the output-coupling region to that at the drop-waveguide as a

figure-of-merit we term the S factor. Our experimental results of four different devices fabricated on SiN-on-silica substrates using two different sized microparticles show good consistency with the proposed design rule, namely that $S > 1$ gives deterministic particle buffering, $S < 1$ gives deterministic particle dropping and $S \approx 1$ leaves the particle transport processes probabilistic. Our numerical modelling suggested that the extracted S factors from transmission spectra are consistent with those extracted from mode-field intensity distributions. We calculated the transverse optical gradient force field distribution in order to explain the deterministic and probabilistic transport processes upon different S factor values. We further realized switching between deterministic particle buffering and probabilistic particle transport processes by tuning the S factor through switching polarization modes. We therefore demonstrated that the S factor provides a clearer physical criterion for determining the particle transport processes compared to the cavity quality (Q) factor.

The SiN microring-resonator-based particle add-drop device can serve as an important building block to route and buffer (bio-) particles on a silicon optofluidic chip²². We envision such a microring-based optofluidic circuit to enable various value-added functionalities for lab-on-chip applications, such as drug synthesis and delivery²³ and trapping with real-time biosensing.²⁴

Acknowledgements

This study was substantially supported by a grant from the Research Grants Council of The Hong Kong Special Administrative Region, China, under project no. 617612. The authors acknowledge the HKUST Nanoelectronics Fabrication Facility for fabricating the optofluidic chip.

References

1. A. Ashkin, *Phys. Rev. Lett.*, 1970, **24**, 156-159.
2. A. Ashkin, J. Dziedzic and T. Yamane, *Nature*, 1987, **330**, 769-771.
3. M. MacDonald, L. Paterson, K. Volke-Sepulveda, J. Arlt, W. Sibbett and K. Dholakia, *Science*, 2002, **296**, 1101-1103.
4. S. Kawata and T. Tani, *Opti. Lett.*, 1996, **21**, 1768-1770.
5. B. S. Schmidt, A. H. Yang, D. Erickson and M. Lipson, *Opt. Express*, 2007, **15**, 14322-14334.
6. S. Gaugiran, S. Gétin, J. Fedeli, G. Colas, A. Fuchs, F. Chatelain and J. Dérourard, *Opt. Express*, 2005, **13**, 6956-6963.
7. A. H. J. Yang and D. Erickson, *Lab Chip*, 2010, **10**, 769-774.
8. S. Lin, E. Schonbrun and K. Crozier, *Nano Lett.*, 2010, **10**, 2408-2411.
9. M. Soltani, J. T. Inman, M. Lipson and M. D. Wang, *Opt. Express*, 2012, **20**, 22314-22326.
10. H. Cai and A. W. Poon, *Opt. Lett.*, 2010, **35**, 2855-2857.
11. H. Cai and A. W. Poon, *Opt. Lett.*, 2011, **36**, 4257-4259.
12. C. Renaut, B. Cluzel, J. Dellinger, L. Lalouat, E. Picard, D. Peyrade, E. Hadji and F. de Fornel, *Sci. Rep.*, 2013, **3**.

13. C. Renaut, J. Dellinger, B. Cluzel, T. Honegger, D. Peyrade, E. Picard, F. De Fornel and E. Hadji, *Appl. Phys. Lett.*, 2012, **100**, 101103.
14. S. Mandal, X. Serey and D. Erickson, *Nano Lett.*, 2009, **10**, 99-104.
15. D. Erickson, X. Serey, Y.-F. Chen and S. Mandal, *Lab Chip*, 2011, **11**, 995-1009.
16. Y.-F. Chen, X. Serey, R. Sarkar, P. Chen and D. Erickson, *Nano Lett.*, 2012, **12**, 1633-1637.
17. H. Cai, J. Wang and A. W. Poon, in *Proceedings of SPIE Photonics West*, 2013, 862904.
18. J. Heebner, R. Grover and T. Ibrahim, *Optical microresonators: theory, fabrication, and applications*, Springer, 2007.
19. I. Brevik, *Phys. Rep.*, 1979, **52**, 133-201.
20. E. Thormann, A. C. Simonsen, P. L. Hansen and O. G. Mouritsen, *Langmuir*, 2008, **24**, 7278-7284.
21. J. Wang and A. W. Poon, in *Proceedings of Conference on Lasers and Electro-Optics (Optical Society of America, 2013)*, 2013, **Paper ATu1N.4**
22. S. Feng, T. Lei, H. Chen, H. Cai, X. Luo and A. W. Poon, *Laser & Photon. Rev.*, 2012, **6**, 145-177.
23. N. Suwanpayak, M. A. Jalil, C. Teeka, J. Ali and P. P. Yupapin, *Biomed. Opt. Express*, 2011, **2**, 159.
24. S. Lin and K. B. Crozier, *ACS Nano*, 2013, **7**, 1725-1730.